Chapter

Modeling of Piezoceramic Actuators for Control

Joel Shields and Edward Konefat

Abstract

In this chapter a full electromechanical model of piezoceramic actuators is presented. This model allows for easy integration of the piezo stack with a structural finite element model (FEM) and includes the flow of energy into and out of the piezo element, which is governed by the transducer constant of the piezo element. Modeling of the piezo stack capacitive hysteresis is achieved using backlash basis functions. The piezo model can also be used to predict the current usage of the PZT which depends on the slew rate of the voltage applied to the PZT. Data from laboratory experiments using a load frame and free response tests is used to estimate the PZT model parameters. In addition, a simplified model of a modulated full bridge strain gauge is derived based on test data which includes the effect of intrinsic bridge imbalance. Sensors of this type are often used with feedback control to linearize the behavior of the device. Taken together, the actuator and sensor model can be used for the development of piezo actuated control algorithms.

Keywords: PZT, transducer constant, strain gauge, hysteresis, charge feedback

1. Introduction

Lead zirconium titanate (PZT) was first developed around 1952 at the Tokyo Institute of Technology. Due to its physical strength, chemical inertness, tailorability and low manufacturing costs, it is one of the most commonly used piezo ceramics. It is used in various applications as an actuator including micromanipulation and ultrasonics. Due to the piezoelectric effect [1], it can also be used as a sensor of force or displacement or for energy harvesting since current is produced by the device in response to an applied strain. Three main issues, however, compromise the utility of these devices. The first is that the stroke of these devices is limited to about 40 μm, which for some applications, necessitates the use of dual stage actuation [2, 3] or inchworm actuators [4] which combine brake PZTs with actuation PZTs to extend the dynamic range of these devices. In addition, PZTs suffer from significant amounts of hysteresis (15 percent of full stroke) and creep which causes drift of the device over time. These two issues make open loop operation of these devices problematic since multiple displacements are possible for the same input and due to the fact that creep dissipates at very slow rates. To overcome these problems, it is possible to invert the hysteresis nonlinearity [5] but this can only improve accuracy by one order of magnitude and leaves the creep issue unresolved. This has led many to employ servo control with displacement sensing of the PZT elongation [6–8]. This will linearize the device to the accuracy of

the sensor, and address creep, but the hysteresis nonlinearity has an impact on the loop stability which must be analyzed. In a linear sense, the hysteresis has an effect on the both the loop gain and phase margin. These impacts necessitate high fidelity modeling of the PZT behavior, which can be quite rich and faceted. The model described in this chapter is intended to be used as a necessary precursor for control design and simulation.

Many models for PZT stacks have been developed in the literature, such as those in [8–10], but few incorporate the transfer of energy into a structure and out of the structure back into the device. Of those that do describe this important detail, [1, 11–13], the treatment of piezoelectric hysteresis in the model is often problematic in that either friction elements, such as the Maxwell resistive capacitor (MRC) are used, which are difficult to simulate, or nonlinear differential equations are used which have very heuristic fitting functions [1]. The hysteresis model described here overcomes these difficulties by using backlash basis functions which are relatively easy to fit to experimental data and are numerically efficient to simulate. The hysteresis model does not included creep, but it is possible to add springs and dashpots to the backlash elements which will capture the creep behavior.

The PZT model presented in this chapter can also be used to predict current usage which is important in terms of amplifier design and slew rate limitations. It can also be easily integrated into a FEM of the structure that the PZT is embedded in. The model in this chapter is based on the work in [1, 12]. Unfortunately, these papers offer little in terms of determining the parameters of the model. In particular, the internal capacitances and transducer constant vary from one type of PZT to another. As a result, this chapter describes experimental techniques for determining these parameters regardless of the particular PZT configuration. We also validate proper operation of our test equipment and compare the simulated model output to test data.

For control design purposes it is also important to model the sensor in addition to the actuator. Various types of sensors have been used for PZT control such as optical encoders with 1.2 nm resolution, laser metrology gauges, and more commonly, strain gauges. Strain gauges offer good performance for the price and can be directly bonded to the sides of the PZT. A model of a modulated full strain gauge bridge is given which includes the effect of intrinsic bridge imbalance and bridge sensitivity. A simplified version of this model, excluding all exogenous signals, is given to facilitate loop shaping of a control loop.

PZTs are often used in optical instrument such as coronagraphs, interferometers, spectrometers and microscopes where micro-manipulation below the scale of optical wavelengths is required. Given the small wavelengths of visible and infrared light (350 nm - 14 μm), subnanometer positioning is required for these applications. PZTs come in a wide variety of shapes and configurations. Here we focus on piezo stack actuators which are the most commonly used. In particular, we tested and modeled the P-888.51 PICMA stack multilayer piezo actuator [14] which is ubiquitous in its use for various missions at JPL. This PZT has dimensions of 10 mm $\times$ 10 mm $\times$ 18 mm and has a nominal stroke of 15 μm at 100 Volts across its terminals. It has a blocking force of up to 3600 Newtons and a mechanical stiffness of 200 $N/\mu m$. Nominal voltage range applied to the PZT is 0–100 Volts, but it is possible to apply between -20 - 120 Volts for extended stroke. These devices are operated with large preloads to keep the device in compression during operation. Dynamic loads that put the ceramic device in tension need to be avoided since they are brittle and fracture easily in tension. The recommended preload is 15 MPa which for the 10 mm $\times$ 10 mm cross sectional area of the device is 1500 Newtons. The first mode of this particular PZT is 70 kHz which is far greater than the first mode of any structure it is generally incorporated into.

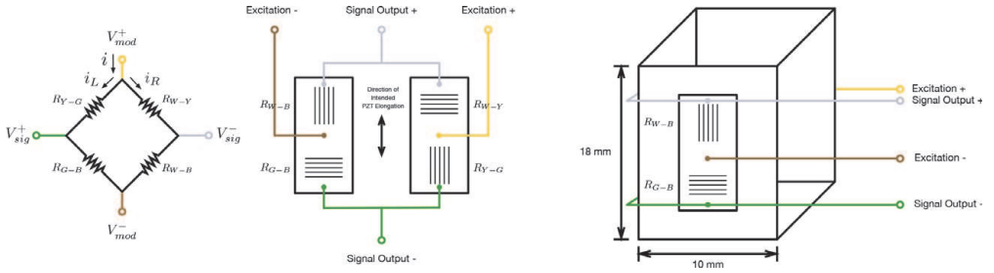

Figure 1.
From left to right, circuit diagram of strain gauge Wheatstone bridge showing resistive elements labeled by the color of wires on each side of the resistor, physical layout of resistive elements and wiring connections, and strain gauge elements bonded to the PZT.

The PICMA P-888.51 can be ordered with a full bridge strain gauge bonded directly to the sides of the PZT ceramic. As mentioned above, strain gauges are used to linearize the hysteretic behavior of PZTs and to mitigate their drift or creep, which can be substantial. To determine the bridge response, we analyze the modulating electronics used to read the Wheatstone bridge. The modulation is a technique commonly used for rejection of noise picked up along the cabling between the PZT and electronics board. The strain gauge bridge we analyze is composed of two Vishay half bridges (Part number N2A-XX-S053P-350) bonded to opposite sides of the PZT as shown in **Figure 1**. Each bridge resistor has a nominal resistance of 350 Ohms.

Three identical PZTs were tested which we refer to by their serial numbers, SN637, SN629 and SN618.

2. Full electro-mechanical PZT model

The PZT model we analyze is depicted in **Figure 2**. It is taken from the model proposed in [1, 12, 13] with a few modifications. We have added a resistor on the input since this is part of the amplifier used to drive the device. We depict the resistor in **Figure 2** as having a switch since most of our experiments were conducted without this resistor. This resistor and the equivalent capacitance of the circuit determines the RC time constant of the actuator model. This time constant can vary based on the voltage input (V_{pea}) history due to the nonlinear capacitance, $C_h(\cdot)$. As current, $\dot{q}$, flows into the circuit charge develops across the working

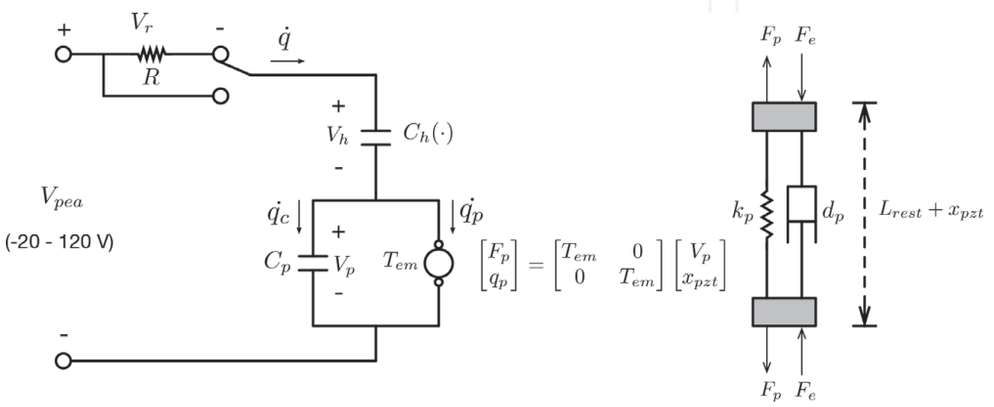

Figure 2.
Nonlinear electro-mechanical PZT model. Features of this model include the nonlinear capacitance, $C_h(\cdot)$, and transducer constant, T_{em}, which governs the flow of energy into and out of the PZT.

capacitor, C_p, which due to the *inverse piezoelectric effect* produces a force, F_p in the piezoelectric stack. Conversely, any environmental force, F_e, which causes velocity of the PZT stack generates a current, $\dot{q}_p$, in the circuit due to the *piezoelectric effect*.

The unknown model parameters in **Figure 2** include the two capacitances, C_p and $C_h(\cdot)$, and the transducer constant, T_{em}. The resistor value, R, is known by design (80 Ohms) and can be easily measured. The mechanical stiffness of the PZT, k_p, can be obtained from Physik Instrumente (PI) spec. Sheets [14]. The damping coefficient, d_p, of the PZT ceramic is a structural parameter of the PZT and not part of this investigation. It is primarily a parameter that effects the high frequency behavior of the PZT in terms of changing the modal response. Here we are more concerned with the low frequency, nonlinear behavior of the device.

Writing some simple circuit equations based on **Figure 2**, we have Kirchhoff's Voltage Law (KVL) and Kirchhoff's Current Law (KCL),

$$V_{pea} = V_r + V_h + V_p \qquad (KVL) \tag{1}$$

$$\dot{q} = \dot{q}_c + \dot{q}_p \qquad (KCL). \tag{2}$$

We also have the three constitutive relations for each of the components in this circuit,

$$q = C_h(V_h) \qquad q_c = C_p V_p \tag{3}$$

$$V_r = i_r R \qquad with \qquad q(t) = \int_0^t i_r(t)dt. \tag{4}$$

Using Eqs. (1)–(4) we can convert the circuit diagram in **Figure 2** to the block diagram in **Figure 3**. **Figure 3** is easier to simulate since the mixed electrical and mechanical domains are irrelevant. Few simulation software applications allow for mixed domain signals. SPICE is a typical example of this. Simscape™ does allow for mixed domain signals but nonlinear multivalued capacitors are not supported. Putting the model in block diagram form allows for easy integration in the Matlab® and Simulink® programming environment which supports simulation of both a structural model for the mechanical impedance, $M(\cdot)$, and hysteretic capacitance, $C_h(\cdot)$, using primitive Simulink components. Looking at **Figure 3** KVL is represented with the first two summing nodes. The center summing node is depicting an integrated version of KCL, Eq. (2). Since the voltage across the resistor, V_r, is proportional to the current, $\dot{q}$, the charge, q, needs to be differentiated, thus we use the Laplace operator, s, in **Figure 3** to represent this. The saturation block on

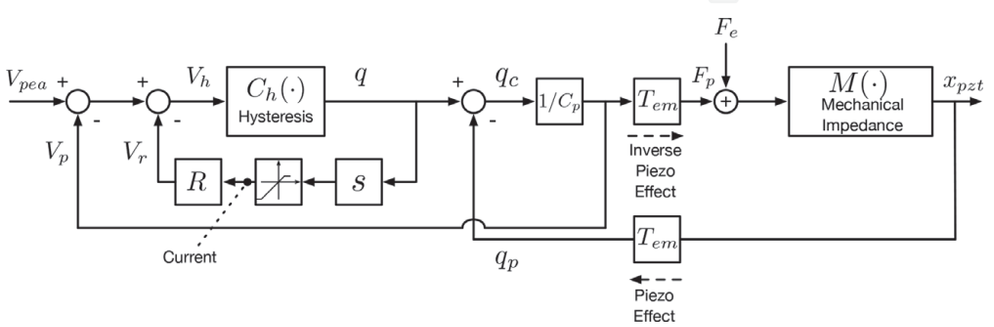

Figure 3.
Block diagram of PZT model showing the inverse piezo effect and piezo effect with charge feedback. The nonlinear capacitance function, $C_h(\cdot)$, is modeled with backlash operators. The mechanical impedance, $M(\cdot)$, can be as simple as a spring representing the mechanical stiffness of the PZT material or a FEM of the structure the PZT is embedded into.

current is included to capture current limits of the PZT amplifier. As an example of this, the flight amplifier for the Nancy Grace Roman Space Telescope has a limit of +2 mA for sourcing of current into the PZT and − 14 mA for sinking of current out of the PZT.

At steady state and with the boundary conditions at both ends of the PZT free (i.e. no structural stiffness to oppose the PZT produced force, F_p.), the mechanical impedance of the PZT, $M(\cdot)$, reduces to $1/k_p$. The displacement of the PZT can then be written as,

$$x_{pzt} = \frac{1}{k_p}\left(F_e + F_p\right), \tag{5}$$

with $F_p = T_{em}V_p$. With the terminals of the PZT open circuit $V_p = V_{pea}$ assuming the device has been shorted and drained of all charge prior to applying an environmental force. Since V_{pea} is a measurable signal this allows us to solve for T_{em} using Eq. (5),

$$T_{em} = \frac{k_p x_{pzt} - F_e}{V_{pea}}, \tag{6}$$

where both x_{pzt} and F_e can also be measured. This equation forms the basis of the experiments described in Section 3.2.

To determine the nonlinear capacitance, $C_h(\cdot)$, and working capacitance, C_p, we collect input/output data while applying a voltage, V_{pea}, to the PZT with the environmental force, F_e, set to zero. To determine the hysteresis of this block over its full range of inputs, we apply a sinusoidal V_{pea} voltage that goes from 0–100 Volts. This voltage is applied slowly so that we can assume that $M(\cdot) \approx 1/k_p$. The output signal of $C_h(\cdot)$, q, can be obtained by integrating measurements of the current flowing into the PZT as a result of the voltage, V_{pea}, applied to the PZT terminals. The input signal to $C_h(\cdot)$, V_h, can be solved for using KVL,

$$V_h = V_{pea} - V_r - V_p, \tag{7}$$

where $V_r = 0$ since during this test the resistor R is not used. V_p in Eq. (7) can be solved for by using Eq. (5) with $F_e = 0$ and $F_p = T_{em}V_p$. This leads to,

$$V_p = \frac{x_{pzt}k_p}{T_{em}} \tag{8}$$

Eqs. (7) and (8) together with the measured charge, q, form the basis of the experiments described in Section 3.3 for determining the nonlinear capacitance, $C_h(\cdot)$.

From the block diagram in **Figure 3** we have,

$$V_p = \frac{1}{C_p}\left(q - T_{em}x_{pzt}\right). \tag{9}$$

Plugging in $F_e = 0$ and $F_p = T_{em}V_p$ with V_p given by Eq. (9) into Eq. (5) we have,

$$x_{pzt} = \underbrace{\frac{T_{em}}{k_p C_p + T_{em}^2}}_{k_{q2x}} q. \tag{10}$$

We can solve for the gain, k_{q2x}, in a least squares sense,

$$k_{q2x} = \left(\mathbf{q}^T\mathbf{q}\right)^{-1}\mathbf{q}^T\mathbf{x}_{pzt} \tag{11}$$

where $\mathbf{q}$ and $\mathbf{x}_{pzt}$ are vectors of the sampled signals q and x_{pzt}. The working capacitance, C_p, is then,

$$C_p = \frac{T_{em} - T_{em}^2 k_{q2x}}{k_p k_{q2x}} \tag{12}$$

Eqs. (10)–(12) form the basis of the experiments described in Section 3.3 for determining the working capacitance, C_p.

The strain gauge voltage change is the difference between the voltage at the start of the test and at the time that the peak force was applied.

3. Experiments

3.1 Displacement sensing for test campaign

Both experiments described below require sensing of the PZT elongation. To do this we use the strain gauge bonded to the PZT. For testing purposes we applied a DC voltage (10 Volts) as the excitation input to the bridge and configured a differential amp on the output of the bridge. The gain of this amplifier was set to 311.4 which amplified the millivolt signal of the bridge output to the 2–3 Volt range which was easily measurable by our test equipment. The amplified voltage was calibrated to the actual displacement of the PZT using a micrometer with 0.5 micron accuracy (Mitutoyo MDH high accuracy digimatic micrometer, series 293.). A linear fit of the calibration data, measured displacement vs. measured voltage, revealed a fit error of 0.71 microns for the worst case PZT with scale factors of 3.077 ($\mu m/V$), 3.183 ($\mu m/V$) and 3.246 ($\mu m/V$) for SN637, SN629 and SN618 respectively. Calibrated steady state measurements of the strain gauge had an RMS of 22 nm which was more than sufficient for our testing campaign.

3.2 Experiment 1: instron testing

As discussed above we use the force balance Eq. (6) to determine the transducer constant, T_{em}. The environmental force, F_e, in this equation was applied using an Instron 8801 Servohydraulic load frame which is part of the JPL Materials Testing and Failure Facility. Refer to **Figure 4** for a picture of the PZT test jig. To avoid potential damage to the load frame the hydraulic press was operated in displacement mode which left force an uncontrolled, but measured parameter (see **Figure 5**). To measure the back EMF term, V_{pea}, in this equation a voltmeter with high input impedance is required. Without a high impedance voltmeter the RC decay time constant would be much faster than the duration of the experiment and compromise the data. We used a Keithley 617 high resistance meter with 200 TeraOhm input impedance to keep charge from bleeding off the PZT leads. To measure the PZT displacement an Agilient 34401A DMM was used to monitor the amplified bridge output voltage. The applied compressive load to the PZT was measured with the load cell that is incorporated into the load frame.

Each of the three PZTs was tested with and without the load resistor to see how much resistive force is created by the charge feedback. Tests done with the resistor

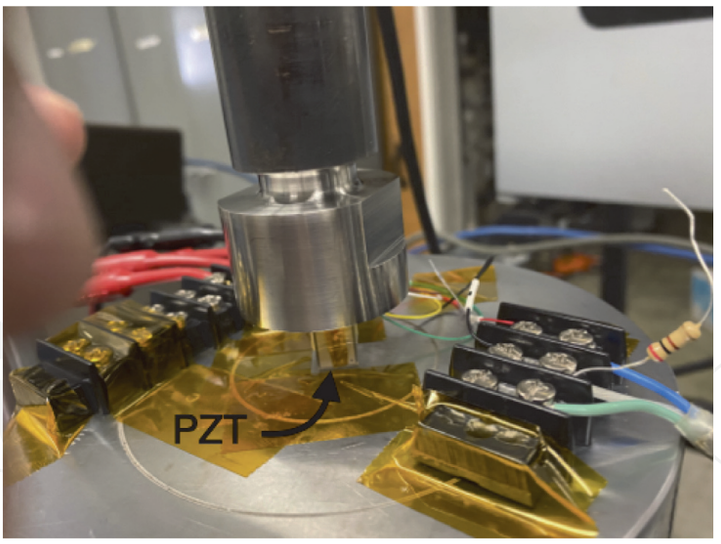

Figure 4.
PZT installed in the Instron jig between two compression platens. The load frame is used to apply a compressive load of 800 (N) while the PZT displacement, back EMF, and applied load are measured. The PZT is compressed with and without a 200 Ohm resistor applied across the leads of the PZT. This resistor is shown on the right terminal block in the open circuit configuration.

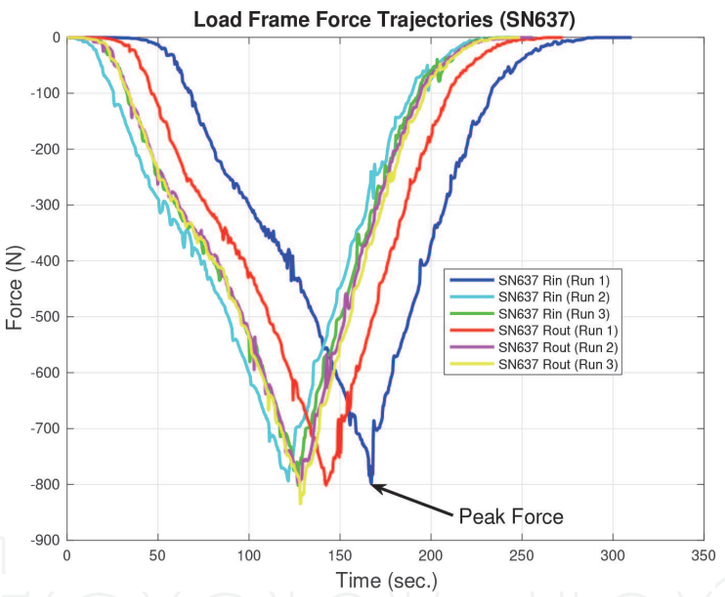

Figure 5.
PZT signal set recorded during each free response test. The charge signal was obtained by integrating the current. The position signal was obtained by sampling the strain gauge voltage and applying the calibration described in Section 3.1.

bleeds off any charge that would otherwise develop and leaves only the mechanical stiffness to oppose the applied compressive force. In addition, to verify repeatability of the experimental results each tested configuration was repeated three times. **Table 1** summarizes the results of these tests. Note that with the load resistor the peak displacements are substantially greater than the cases without the load resistor even though the peak loads applied are similar. This is the result of charge feedback generating an opposing force beyond that provided by the mechanical stiffness alone. It may be surprising to find that the electrical force produced is close to or even greater than the force produced by the mechanical stiffness when the resistor is not used. Plugging in the peak force, Fe, the peak displacement, x_{pzt}, and peak back EMF, V_{pea}, from **Table 1** into Eq. (6), and using the spec. Sheet value [14] of the mechanical stiffness, $k_p = 200\ \ (N/\mu m)$, we can solve for the transducer

R In	SN637	SN637	SN637	SN629	SN629	SN629	SN618	SN618	SN618
	(Run 1)	**(Run 2)**	**(Run 3)**	**(Run 1)**	**(Run 2)**	**(Run 3)**	**(Run 1)**	**(Run 2)**	**(Run 3)**
Strain Gauge Voltage Change (V)	−0.925	−1.040	−0.958	−1.112	−0.918	−0.944	−0.885	−0.914	−0.926
Peak Displacement (um)	**−2.847**	**−3.200**	**−2.949**	**−3.538**	**−2.922**	**−3.006**	**−2.873**	**−2.966**	**−3.005**
Peak Force (N)	−772.2	−778.1	−774.3	−799.5	−738.6	−773.3	−792.8	−798.8	−809.8
Peak Back EMF (V)	0.0	0.0	0.0	0.0	0.0	0.0	0.0	0.0	0.0
R Out	**SN637**	**SN637**	**SN637**	**SN629**	**SN629**	**SN629**	**SN618**	**SN618**	**SN618**
	(Run 1)	(Run 2)	(Run 3)	(Run 1)	(Run 2)	(Run 3)	(Run 1)	(Run 2)	(Run 3)
Strain Gauge Voltage Change (V)	−0.415	−0.413	−0.426	−0.382	−0.381	−0.384	−0.334	−0.334	−1.078
Peak Displacement (um)	**−1.277**	**−1.272**	**−1.311**	**−1.217**	**−1.213**	**−1.221**	**−1.084**	**−1.084**	**−0.336**
Peak Force (N)	−798.8	−797.1	−834.3	−807.2	−795.8	−800.0	−808.8	−815.4	−844.0
Peak Back EMF (V)	11.68	12.32	12.55	11.98	12.51	12.63	12.20	12.21	12.15

Table 1.
Instron testing data with and without load resistor. For each PZT, SN637, SN629 and SN618 the load test was repeated three times.

constant, T_{em}. The mean value of T_{em} over each PZT and over the three runs for each PZT was 46.71 (N/V) or (C/m). The variance of this estimate was minimal.

3.3 Experiment 2: free-free test

To perform the free-free test on the PZT, the applied voltage, resulting current applied to the PZT and PZT displacement all need to be measured synchronously. To do this we used a Keysight Technologies B2902A precision source to sample the applied voltage and current. This instrument was designed to measure I/V measurements easily and accurately. To measure the PZT displacement the output of the bridge differential amp was measured with a Tektronics oscilloscope. To synchronize the two data sets we used the peak value in each data record. These signals are shown in **Figure 5** together with the applied charge which is just the integrated current. Before each test a relay was used to temporarily short the leads of the PZT to drain any charge. This put the PZT in its rest state prior to each test.

To validate our instrumentation we compared the current and charge reported by our test setup using a simple 5.5 μF capacitor against a SPICE simulation with the same capacitor value. The peak charges agreed to within 2 percent providing confidence to the current measurements.

Using the PZT position and charge measurements shown in **Figure 6** along with the previously estimated value of the transducer constant, T_{em}, and stiffness, k_p, taken from the PI spec. Sheet [14], we can use Eqs. (10)–(12) to solve for the working capacitance, C_p. This resulted in a value of 5.802 μF for SN637 which is close to the small signal (1 V_{pp}) effective capacitance value listed in the PI spec. Sheet of 6.0 $\mu F \pm 20\%$. Note the effective capacitance in our model is the series

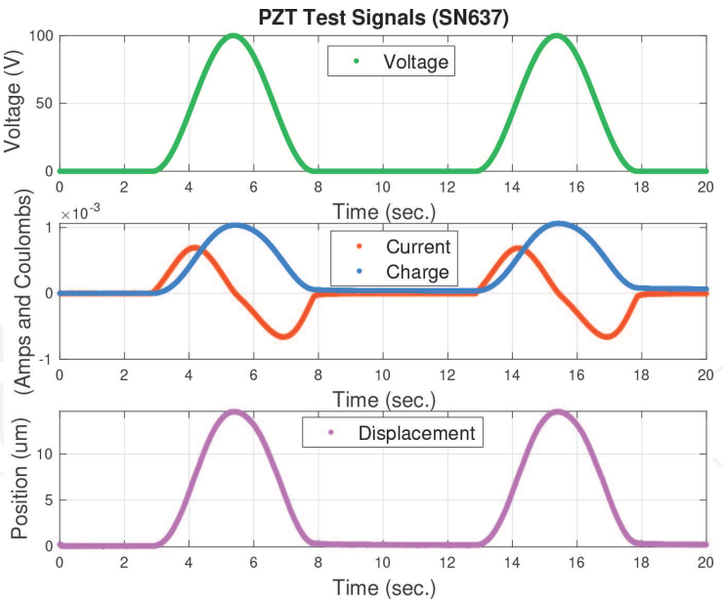

Figure 6.
Force trajectories during operation of the load frame in displacement mode. Each of the three PZTs was tested three times with the load resistor, R_{in} cases, and three times without the load resistor, R_{out} cases. Since force was not a controlled variable during the test it had a noticeable but tolerable amount of variation or jitter.

combination of C_p with $C_h(\cdot)$ which is $C_pC_h(\cdot)/\left(C_p + C_h(\cdot)\right)$. Thus, whatever the value of $C_h(\cdot)$ it can only act to reduce the effective capacitance from the baseline value of C_p.

Before determining the nonlinear function, $C_h(\cdot)$, the input signal, V_h, is generated using Eqs. (7) and (8). This revealed that the voltage drop across the hysteretic capacitance, V_h, was approximately one-third of the applied voltage, V_{pea}. This leaves two-thirds of the applied voltage across the working capacitor to produce work. The output of the nonlinear function, $C_h(\cdot)$, is given by the charge measurements, q. The input and output data is shown in **Figure 6** which demonstrates a great deal of hysteresis. Note that creep between the two applied sinusoids infects the data as can be seen in the lower left of **Figure 7**. This portion of the data was not fit by the model described below.

3.3.1 Hysteresis model

To fit the capacitive hysteresis data a neural network of backlash basis functions is employed of the form,

$$q = \sum_{i=1}^{N} B_i\left(V_h, x_i^o, w_i\right) \cdot k_i \tag{13}$$

where $B_i\left(V_h, x_i^o, w_i\right)$ is a backlash operator with input variable, V_h, initial condition, x_i^o, and deadband width, w_i. Each backlash output is weighted with a gain k_i which changes the slope of the backlash operator when the deadband is engaged. Details of fitting the parameters of this model to experimental data are given in [5, 15] but, to summarize, the gains k_i are used to fit the curvature of the hysteresis data, the schedule of deadband widths, w_i, are used to accurately capture regions of the hysteresis that have high curvature and the initial conditions are used to capture the uniqueness of the initial loading curve. A diagram of the hysteresis model is provided in **Figure 8**.

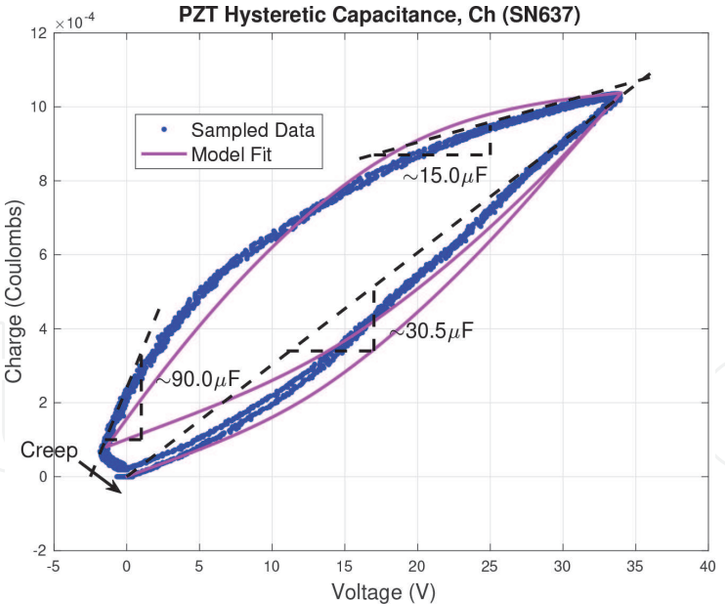

Figure 7.
Capacitive hysteresis data and model fit. Linearized approximations are shown with the large signal approximation of ~30.5 μF.

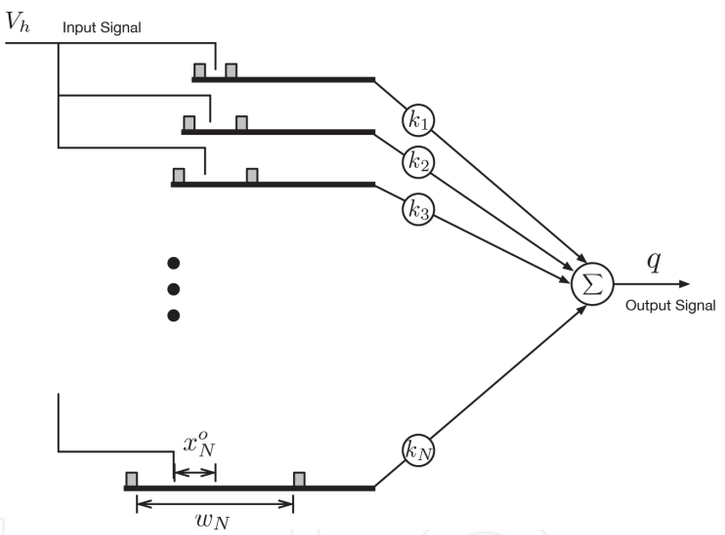

Figure 8.
*Diagram of capacitive hysteresis model used to fit the data in **Figure 7**. Initial state and deadband width are indicated for the Nth element of the model. The output arm displacement of each backlash element is multiplied by gain k_i and summed with the other backlash elements to form the output variable q.*

4. Complete model

To validate the PZT model described in this chapter we exercise the model in **Figure 3** by applying a full scale (0–100 Volt) sinusoidal input voltage, V_{pea}, and record the model output, x_{pzt}. This data can then be compared with the same data acquired during the experiments described in Section 3.3. This comparison is made in **Figure 9** which shows good agreement between the experimental data and model data. In addition, comparisons of the experimentally measured current and modeled current signal also demonstrated similar agreement. Note the hysteresis percentage in **Figure 9**, as defined by the vertical thickness of the hysteresis loops relative to the peak displacement, is lessened for the output signal of the model relative to the percentage of hysteresis demonstrated in **Figure 7**. This is most likely

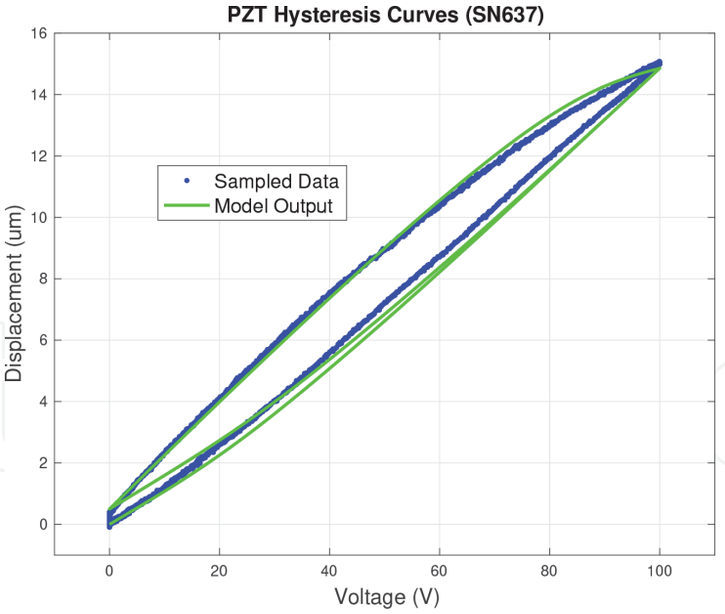

Figure 9.
Experimental and modeled input/output data for the full PZT model.

due to the voltage feedback terms, V_p and V_r, in **Figure 3** that act to reduce the uncertainty caused by the capacitive hysteresis, $C_h(\cdot)$.

5. Modulated strain gauge model

We have seen from the test data that the behavior of the PZT is nonlinear due to its hysteresis. Many applications of PZT actuators require greater positioning accuracy than what can be achieved with open loop operation of the PZT. To overcome this accuracy issue, it is common to use strain gauges bonded directly to the face of the PZT. These sensors are used with feedback control to greatly improve the positioning accuracy of the actuator. Typically the accuracy can be improved from 12–15 percent down to 0.1 percent by using strain gauge sensors. Strain gauge sensors also suffer from hysteresis (This is what limits their accuracy.) but the amount of hysteresis is much less than the actuator.

Before designing any control loop that uses strain gauge feedback, it is necessary to understand the output response of the strain gauge voltage versus the input strain. To do this, we first characterize the resistive changes of the four Wheatstone bridge resistors as a function of the PZT elongation. The results of this analysis can then be used to derive the sensitivity of the bridge output. This analysis assumes that the strain gauge bridge is modulated with a square wave reference at its excitation terminals. The modulation is done in order to reduce noise pickup in the cabling between the bridge location and PZT processing electronics board which can be separated by several meters in typical applications. Any noise with a frequency content well below the modulation frequency of 10 kHz can be eliminated with this technique. Demodulation can be done in analog electronics but here we describe a case where the demodulation is done in FPGA firmware.

5.1 Bridge resistance changes

The stain gauge configuration we study is a full Wheatstone bridge, meaning that all four resistive elements of the bridge see a change in strain due to the elongation of the PZT. Two of the bridge elements, on opposite diagonals of the

Wheatstone bridge, are bonded to the PZT along the length of the PZT which is the direction of intended length change. The remaining two bridge elements are bonded to the PZT perpendicular to this, along the width of the actuator. These two bridge elements will also see a resistance change when the PZT elongates due to the fact that as the PZT lengthens it also gets more narrow. The circuit diagram of the Wheatstone bridge and layout of the bridge elements when bonded to the PZT is shown in **Figure 1**.

To characterize the exact relationship between the PZT elongation and resistive change of each bridge element we conducted a test where the resistance measurement across each strain gauge resistor was measured for several increments of PZT displacement from its rest length to its maximum displacement. Each resistance measurement is the equivalent resistance of the element across the probe terminals in parallel with the other three elements, i.e.,

$$R_{m1} = R_{W-Y} \| R_{Y-G} + R_{G-B} + R_{W-B} \tag{14}$$

$$R_{m2} = R_{W-B} \| R_{W-Y} + R_{Y-G} + R_{G-B} \tag{15}$$

$$R_{m3} = R_{G-B} \| R_{W-B} + R_{W-Y} + R_{Y-G} \tag{16}$$

$$R_{m4} = R_{Y-G} \| R_{G-B} + R_{W-B} + R_{W-Y}. \tag{17}$$

These measurements must be solved for the individual bridge elements by solving the system of equations in (14)–(17) for each of the four bridge element resistances. This system of equations is nonlinear but can be solved uniquely using a nonlinear equation solver. Mathematica was used for this purpose. Solving this system of equations resulted in three complex solutions and one real solution for each of the resistances on the right hand side. Since the resistance must be real, the real solution was taken as the answer.

The results of these measurements are shown in **Figure 10** for PZT SN618. The two strain gauges that are oriented along the length of the PZT increase their resistance as the PZT elongates since this deformation lengthens the gauge and thins the wires of the bridge. The two strain gauges oriented along the width of the PZT

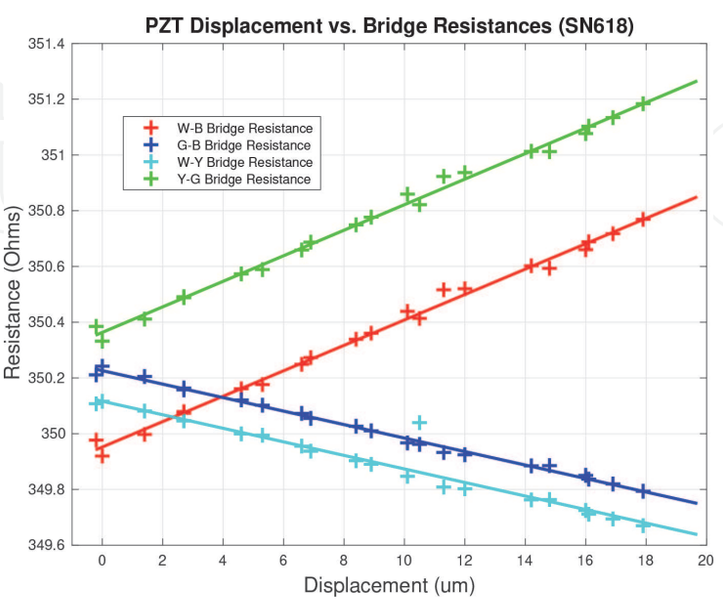

Figure 10.
Four bridge resistances as a function of PZT displacement. This data is from 1 of 3 PZTs tested. Note the difference in slopes of the four resistors, one negative slope for the two horizontally placed bridge elements and one positive slope for the two vertically placed bridge elements. Initial resistances at zero elongation reveals the intrinsic bridge imbalance due to manufacturing tolerances.

decrease in resistance since, in this direction, the PZT narrows. As it narrows the wires of these bridge resistors become shorter and thicker reducing their resistance. Interestingly, the ratio of the slopes of the horizontally mounted gauges to the vertically mounted gauges is equal to the aspect ratio of the PZT, W_{rest}/L_{rest}, where W_{rest} is the rest width of the PZT and L_{rest} is the rest length of the PZT. Also note that at zero elongation of the PZT, the actual resistance of each bridge element deviates from the nominal value of 350 Ohms. For all three full bridge strain gauges tested the variation from the nominal resistance for each bridge element was found to be 0.224 Ohms, 1-σ with a maximum error bounded by ± 0.4 Ohms. This was consistent with the spec. Sheet tolerance [16].

Taking into account the nominal resistance, variation in nominal resistance and strain induced resistance change, the resistance of each bridge element can be written as,

$$R_{W-Y} = \left(R_{nom} + \Delta R_{nom}^{W-Y}\right) - k_{gf} \cdot \left(R_{nom} + \Delta R_{nom}^{W-Y}\right) \cdot \left(\frac{1}{L_{rest}}\right) \cdot \left(\frac{W_{rest}}{L_{rest}}\right) \cdot s_{pzt} \quad (18)$$

$$R_{G-B} = \left(R_{nom} + \Delta R_{nom}^{G-B}\right) - k_{gf} \cdot \left(R_{nom} + \Delta R_{nom}^{G-B}\right) \cdot \left(\frac{1}{L_{rest}}\right) \cdot \left(\frac{W_{rest}}{L_{rest}}\right) \cdot s_{pzt} \quad (19)$$

$$R_{Y-G} = \left(R_{nom} + \Delta R_{nom}^{Y-G}\right) + k_{gf} \cdot \left(R_{nom} + \Delta R_{nom}^{Y-G}\right) \cdot \left(\frac{1}{L_{rest}}\right) \cdot s_{pzt} \quad (20)$$

$$R_{W-B} = \left(R_{nom} + \Delta R_{nom}^{W-B}\right) + k_{gf} \cdot \left(R_{nom} + \Delta R_{nom}^{W-B}\right) \cdot \left(\frac{1}{L_{rest}}\right) \cdot s_{pzt}, \quad (21)$$

where k_{gf} is the *gauge factor* of the bridge element ($k_{gf} = 2.05$ [11]) which relates the change in resistance to the strain, (s_{pzt}/L_{rest}). R_{nom} is the nominal bridge resistance and $\Delta R_{nom}^{W-Y}, \Delta R_{nom}^{G-B}, \Delta R_{nom}^{Y-G}, \Delta R_{nom}^{W-B}$ are the variations from this nominal value. In the following treatment of bridge sensitivity, these intrinsic imbalance terms can be ignored since they are a small portion of the total resistance.

5.2 Bridge sensitivity

Referring to **Figure 9** we can derive the bridge sensitivity using simple circuit analysis. Writing out the constitutive relation for each resistor we have,

$$V_{mod}^{+} - V_{sig}^{+} = i_L \cdot R_{Y-G} \quad (22)$$

$$V_{mod}^{+} - V_{sig}^{-} = i_R \cdot R_{W-Y} \quad (23)$$

$$V_{sig}^{+} - V_{mod}^{-} = i_L \cdot R_{G-B} \quad (24)$$

$$V_{sig}^{-} - V_{mod}^{-} = i_L \cdot R_{Y-G}, \quad (25)$$

where i_L and i_R are the currents indicated in **Figure 1**. Solving this system of equations for i_L, i_R, V_{sig}^{+} and V_{sig}^{-} as functions of the two excitation voltages V_{mod}^{+} and V_{mod}^{-} gives the output voltage, $V_{out} = V_{sig}^{+} - V_{sig}^{-}$, as,

$$\begin{aligned} V_{out} = V_{sig}^{+} - V_{sig}^{-} = &\frac{R_{W-B}}{R_{W-B} + R_{W-Y}} V_{mod}^{+} + \frac{R_{W-Y}}{R_{W-B} + R_{W-Y}} V_{mod}^{-} \\ &- \frac{R_{G-B}}{R_{G-B} + R_{Y-G}} V_{mod}^{+} - \frac{R_{Y-G}}{R_{G-B} + R_{Y-G}} V_{mod}^{-}. \end{aligned} \quad (26)$$

Substituting the resistances, Eqs. (18)–(21), into Eq. (26) and letting $V_{mod}^{+} = V_{mod}$ and $V_{mod}^{-} = -V_{mod}$ we can express the output voltage of the bridge as a function of the displacement x_{pzt},

$$V_{out} = f(s_{pzt}) = \frac{2V_{mod}k_{gf}(L_{rest} + W_{rest})x_{pzt}}{\left(2L_{rest}^2 + k_{gf}L_{rest}x_{pzt} - W_{rest}k_{gf}x_{pzt}\right)}. \tag{27}$$

Note that the output voltage of the Wheatstone bridge is actually weakly nonlinear in the PZT displacement, x_{pzt}, which is a bit surprising. Also note that the signal level of the output is directly proportional to the modulation voltage, V_{mod}. This implies that the resolution of the device can be arbitrarily increased with larger excitation voltages. The cost of this increased resolution would be an increased thermal signature. The thermal signature can be an issue in some applications since it can cause excessive drift of the electronics and warping of any optics near the bridge.

To derive the linearized gain of Eq. (27), we can use the first term of a Taylor series,

$$\frac{V_{out} - f(x_{pzt_o})}{x_{pzt} - x_{pzt_o}} = \left.\frac{\partial f}{\partial x_{pzt}}\right|_{x_{pzt}=x_{pzt_o}} = \left.\frac{\left(4L_{rest}^2 V_{mod}k_{gf}x_{pzt}(L_{rest} + W_{rest})\right)}{\left(2L_{rest}^2 + k_{gf}L_{rest}x_{pzt} - k_{gf}W_{rest}x_{pzt}\right)^2}\right|_{x_{pzt}=x_{pzt_o}}. \tag{28}$$

Evaluating this derivative at $x_{pzt_o} = 7.5(\mu m)$ gives a gain of 354.18 (V/m) between the change in PZT elongation from x_{pzt_o} and the change in differential bridge output voltage, $V_{out} - f(x_{pzt_o})$.

5.3 Simplified model

After the bridge, a differential amplifier is used to boost the voltage to the ±2.5 Volt range of the A2D converter (COBHAM RAD1419 with 14 bits). This sampling is done at high rate, 800 kHz, to capture the high and low modulation levels of the 10 kHz square wave. This gives 40 samples during each portion of the modulation signal. These samples are averaged and then differenced before being operated on in firmware. The FPGA firmware applies a linear transformation to this signal in order to map it to the desired DAC range of ±2.6 Volts for the feedback servo. This bias

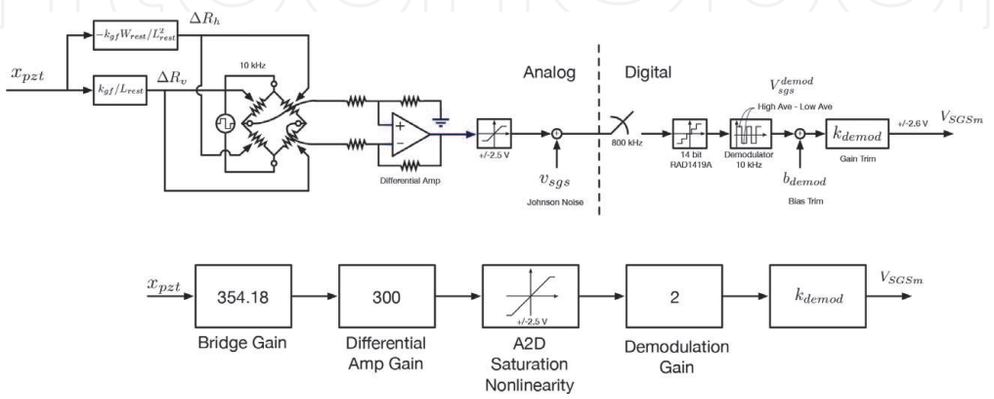

Figure 11.
Circuit schematic (top subfigure) and simplified block diagram of the strain gauge processing electronics (bottom subfigure). Modulation of the Wheatstone bridge is done with a 10 kHz square wave with 2 Volts applied to the reference excitation terminal and − 2 Volts applied to the reference ground terminal. These voltages are swapped every 50 usec. The bridge voltages are sampled at 800 kHz and demodulated in firmware.

and scale factor trimming can be done in analog electronics but is more accurately done in firmware. The full signal chain from PZT displacement to demodulated firmware voltage is shown in the top subfigure of **Figure 11**. The gain of the differential amp cannot map its output voltage exactly to the rails of the A2D since the intrinsic imbalance of the gauge and resulting bias voltage at zero PZT displacement prevents this.

For purposes of control loop design a simplified model of the strain gauge response is useful. If we ignore exogenous signals, such as the gauge noise and bias trim, which do not effect the loop gain, a simplified linear model of gauge response is shown in the bottom subfigure of **Figure 11**. The bridge gain, the differential amp gain of 300, demodulation gain of 2 and trim scale factor are all indicated in this figure. The demodulation gain is 2 since the firmware takes the difference between the same two voltages with opposite sign. Eqs. (27) and (28) give the sensitivity of each of these voltage levels and not their difference.

6. Conclusions

In this work we have developed a full electro-mechanical model of piezoelectric actuators and determined the parameters of this model. Unique experiments were designed to determine the transducer constant and capacitances of the model. The hysteretic capacitance was fit with backlash basis functions which was proposed by the first author in [15]. This hysteresis model is numerically efficient and captures the multivalued behavior of hysteresis as well as the curvature of the hysteresis loops. The output of the PZT model agreed well with the experimental data and successfully predicts the current draw of the actuator which is an important feature of the model for comparison against power limits and slew rate requirements.

For control design actuator models are only half of what is required. Models of the sensors used is also important. In this work we focused on the use of strain gauge sensors which are commonly used with PZT actuators. A nonlinear model of the strain gauge full bridge was developed from which a linearized model was generated. This linear model included the effects of Wheatstone bridge sensitivity, differential amplification, demodulation and firmware scaling.

Although not the focus of this work, the PZT model that we have developed and experimentally identified could easily be included into a FEM of the structure that the PZT is intended to move. This has been done for the fast steering mirror (FSM) used by the Nancy Grace Roman Space Telescope. This FSM has three PZTs that are used to actuate special flexures that amplify the PZT elongation. This amplified motion is used to move a mirror flat in tip, tilt and piston.

One issue that is often over looked with piezo devices is the creep that is produced by these devices. This makes open loop operation with these actuators very challenging. With sensing the creep is usually slow enough to be effectively cancelled by using feedback. Nonetheless, a full piezo model with creep has not been successfully developed to the knowledge of the authors. Augmentations to the backlash elements presented in this work have shown promise in this area but further investigations are necessary.

Acknowledgements

The work described in this paper was carried out at the Jet Propulsion Laboratory, California Institute of Technology, under contract with the National

Aeronautics and Space Administration. The author wishes to thank the Nancy Grace Roman Space Telescope Project for funding this work.

Conflict of interest

The authors declares no conflict of interest.

Author details

Joel Shields* and Edward Konefat
Jet Propulsion Laboratory, California Institute Technology, Pasadena, CA, USA

*Address all correspondence to: Joel.f.shields@jpl.nasa.gov

References

[1] Adriens H, De Koning WL, Banning R. Modeling of Piezoelectric Actuators. IEEE Transactions on Mechantronics. 2000;**5**(4):331-341

[2] Lurie B, Hench J, Ahmed A, Hadaegh F. Nonlinear Control of the Optical Delay Line Pathlength. Orlando: SPIE AeroSense; 1999. pp. 1-11

[3] Atsumi T, Nakamura S, Furukawa M, Naniwa I, Xu J. Triple-Stage-Actuator System of Head-Positioning Control in Hard Disk Drives. IEEE Transactions on Magnetics. 2013;**49**(6):2738-2743

[4] Shields J. Asynchronous Control of a Prototype Inchworm Actuator: Control Design and Test Results. Actuators. 2019;p. 1–21.

[5] Shields J. Characterization and Inversion of the AMD Primary and Secondary Rigid Body Actuators. Pasadena, (CA): Jet Propulsion Laboratory; 2010. D-60616.

[6] Yan Z, Sun L. Design, Control and Application of a PZT-driven Micro-stage. In: International Conference on Mechatronics and Automation. IEEE: Harbin, China; 2007

[7] Zheng J, Fu M. Saturation Control of a Piezoelectric Actuator for Fast Settling-Time Performance. IEEE Transactions on Control Systems Technology. 2013;**21**(1):220-228

[8] Wu Z, Chen M, He P, Li H, Zhang Q, Xiong X, et al. Tracking Control of PZT-Driven CompliantPrecision Positioning Micromanipulator. IEEE Access. 2020;**8**: 126477-126487

[9] Segalman DJ, Starr MJ. Inversion of Masing models via continuous Iwan systems. International Journal of Non-Linear Mechanics. 2008;**43**:74-80

[10] Xiao S, Li Y. Modeling and High Dynamic Compensating the Rate-Dependent Hysteresis of Piezoelectric Actuators via a Novel Modified Inverse Preisach Model. IEEE Transactions on Control Systems Technology. 2012;**21**(5):1549-1557

[11] Lee SH, Royston TJ. Modeling Piezoceramic Transducer Hysteresis in the Structural Vibration Control Problem. The Journal of the Acoustical Society of America. 2000;**108**(6): 2843-2855

[12] Goldfarb M, Celanovic N. Modeling Piezoelectric Stack Actuators for Control of Micromanipulation. IEEE Control Systems Magazine. 1997;**17**(3): 69-79

[13] Liu Y, Shan J, Gabbert U, Qi N. Hysteresis and Creep Modeling and Compensation for a Piezoelectric Actuator Using a Fractional-order Maxwell Resistive Capacitor Approach. Smart Materials and Structures. 2013;**22**: 1-12

[14] PICMA® Stack Multilayer Piezo Actuators [PDF Document]. Physik Instrumente;. Available from: https:// www.pi-usa.us/en/products/piezo-actuators-stacks-benders-tubes/p-882-p-888-picma-stack-multilayer-piezo-actuators-100810/#specification.

[15] Shields J, Sirlin S, Wette M. Starlight Pointing Subsystem for the Formation Interferometer Testbed (FIT). Big Sky, MT: IEEE Aerospace Conference; 2002. pp. 1-11

[16] Vishay Precision Group. Transducer-Class Strain Gauges [PDF Document]. Raleigh, NC 27611: Micro-Measurements;. Available from: https: // www.micro-measurements.com.